

Role of Disorder in Governing the Magnetic Properties of Cu_2IrO_3

Priyanka Yadav¹, Sumit Sarkar², Vishal Kumar³, Sanjay Singh³, Martin A Karlsen⁴, Martin Etter⁴, Sourav Chowdhury⁴, Subhajit Nandy⁴, Yogesh Singh¹

¹Department of Physical Sciences, Indian Institute of Science Education and Research (IISER) Mohali, India

²Department of Physics and Astronomy, University of Waterloo, Waterloo, Canada

³School of Materials Science and Technology, Indian Institute of Technology (BHU), Varanasi-221005, India

⁴Deutsches Elektronen-Synchrotron DESY, Notkestr.85, 22607 Hamburg, Germany

Cu_2IrO_3 is a honeycomb iridate which has been studied recently as a candidate Kitaev quantum spin liquid. Its magnetic ground state however, has been reported to be quantum disordered, spin glassy, or magnetically ordered depending on synthesis details. We have prepared a Cu_2IrO_3 sample with large antisite disorder and studied in detail its structure (global and local), charge states, and thermodynamic properties to try to quantify and characterize the disorder and its connection to the magnetic ground state. X-ray diffraction, Extended x-ray absorption fine structure(EXAFS) and X-ray pair distribution function analysis revealed a large site disorder ($\sim 25\%$), while XPS and XANES reveal mixed valence of Cu and Ir following $\text{Cu}^{1+} + \text{Ir}^{4+} \rightarrow \text{Cu}^{2+} + \text{Ir}^{3+}$. This combination of site disorder and charge redistribution generates competing antiferromagnetic interactions and magnetic frustration, resulting in dynamically fluctuating AFM clusters near 80 K that freeze below 29 K. These results demonstrate the crucial role of synthesis dependent disorder in determining the magnetic ground state of Cu_2IrO_3 .

INTRODUCTION

In recent years, there has been a surge of interest in quasi-two-dimensional (2D) honeycomb iridates and ruthenates as promising candidates for realizing the Kitaev quantum spin liquid (QSL) ground state. The basic ingredients to realize the quantum spin liquid (QSL) state in these materials are the presence of strong spin-orbit coupling (SOC), which gives rise to a pseudo-spin $J_{\text{eff}} = \frac{1}{2}$ state, and the edge-sharing octahedral network that fosters bond-dependent anisotropic Ising exchange interactions leading to frustration [1–4]. The leading candidate materials such as Na_2IrO_3 , $\alpha\text{-RuCl}_3$, and $\alpha\text{-Li}_2\text{IrO}_3$ however, also exhibit additional interactions such as isotropic Heisenberg exchange (often extending beyond nearest neighbors) and off-diagonal exchange [5–7] leading to long-range magnetic order at low temperatures [5, 7, 8]. The quest for an ideal Kitaev material has led to the synthesis of second generation Kitaev materials including Cu_2IrO_3 , $\text{H}_3\text{LiIr}_2\text{O}_6$, and $\text{Ag}_3\text{LiIr}_2\text{O}_6$. These compounds are derived from the first generation Kitaev materials $A_2\text{IrO}_3$, through subtle structural modifications. For example, $\text{H}_3\text{LiIr}_2\text{O}_6$ is obtained by replacing the interlayer Li^+ ions in $\alpha\text{-Li}_2\text{IrO}_3$ with H^+ , while preserving the integrity of the honeycomb layer. Whereas in Cu_2IrO_3 , all A-site cations in Na_2IrO_3 are replaced with Cu, which occupy positions both at the center of the honeycomb and between the honeycomb layers [9–12]. A key feature of these structures is the increase in interlayer separation where the c -axis is elongated via O-Cu-O, O-H-O, or O-Ag-O dumbbell bonds bringing them closer to an ideal configuration with Ir-Ir-Ir bond angles approaching 120° and Ir-O-Ir angles nearing 90° [12]. However, in these intercalated compounds, structural disorders play an important role because of the uncontrolled location of

intercalated ions whose positions strongly affect the local magnetic interactions [13] and can obscure the true magnetic ground state [14, 15], sometimes leading to disorder driven phases which mimic quantum spin liquid behavior [15, 16]. An initial study on Cu_2IrO_3 revealed local moment behaviour with a spin glass like anomaly at 2.7 K suggesting weak disorder [12]. Subsequently, studied materials had varying amounts of disorder at Ir and Cu sites in honeycomb layer leading to differences in magnetic behavior at low temperatures ($T < \theta_{cw}$). Whereas a sample with $\sim 5\text{--}8\%$ disorder showed random singlet behavior in susceptibility measurements at low temperatures and only dynamic fluctuating moments in muon spin relaxation(μSR) [10], a sample with $\sim 20\%$ mixed $\text{Cu}^{1+/2+}$ and $\text{Ir}^{3+/4+}$ charge states revealed both static and dynamic spins in different volumes of the sample [11]. These studies on the one hand point to the possibility of smaller non-Kitaev interactions leading to the absence of magnetic order and a QSL like state despite its Curie-Weiss temperature and effective magnetic moment being similar to those of Na_2IrO_3 [10–12, 17]. On the other hand they point to the role of disorder in deciding the magnetic ground state. Recently the magnetic properties of Cu_2IrO_3 synthesized at lower temperature using CuCl-KCl eutectic salts has been reported [14]. Using this method the synthesis temperature was lowered from 350°C to 170°C. This resulted in samples with 5% Cu/Ir site disorder and magnetic susceptibility revealed a weak ferromagnetic anomaly around 70 K. These reports emphasize the crucial role of chemical disorder in Kitaev materials.

A recent density functional theory (DFT) study has proposed that the mixed valence could lead to long-range charge order with alternate Ir^{4+} and Ir^{3+} on the honeycomb lattice Cu_2IrO_3 [18]. The study also showed

that while in the higher symmetry structure $C2/m$ crystallographic constraints suppress the tendency towards charge-order, the lower symmetry $C2$ phase energetically favors charge ordering albeit with a small energy gain ≈ 4 meV/f.u. With such a low energy gain, its stabilization in real materials is likely hindered by factors such as stacking faults, entropy, and geometric frustration. Consequently, the system may adopt a disordered or glassy distribution of locally mixed valent Ir ions, which preserves the average $C2/m$ symmetry in diffraction measurements [18]. The crystal structure and chemical disorders in the layered materials are highly sensitive to synthesis conditions. Factors like temperature, synthesis atmosphere, and annealing time can significantly influence phase formation, structural integrity, and cation ordering in these systems [19–21].

In the present study, we synthesized Cu_2IrO_3 by employing a prolonged topotactic reaction at 320 °C. Structural refinement revealed an increased cation (chemical) disorder of approximately 25%. The extent and spatial distribution of this disorder were quantified using complementary local structure probes such as extended X-ray absorption fine structure (EXAFS) and X-ray pair distribution function (PDF) analyses. Both techniques provided detailed insight into the local atomic environment, revealing a coexistence of ordered and disordered regions within the honeycomb plane. To quantify the antisite disorder EXAFS and PDF data were modeled using two structural components, one comprising of well-ordered $\text{Cu}^{1+}\text{-Ir}^{4+}$ honeycomb network and other exhibiting Cu-Ir site exchange within the honeycomb lattice. The degree of disorder was quantified from model fits based on the $C2/c$ crystal structure. To further probe the charge configuration associated with this disorder, X-ray photoemission spectroscopy (XPS) and X-ray absorption near-edge structure (XANES) measurements were performed. These results confirmed the presence of mixed oxidation states of Cu and Ir, indicating local charge redistribution accompanying the cation disorder. In the ideal honeycomb structure, Ir^{4+} moments experience Kitaev type bond dependent interactions, which can drive a quantum spin liquid (QSL) state. However, cation site disorder disrupts this framework by introducing Cu-Ir site swapping, which leads to an additional source of frustration. Specifically, when Cu and Ir swap positions, local triangular motifs can emerge within the lattice leading to additional exchange pathways of the type $\text{Cu}^{2+}\text{-O-Ir}^{4+}$ in addition to the usual $\text{Ir}^{4+}\text{-O-Ir}^{4+}$. This potentially introduces competing magnetic interactions that contribute to spin frustration. Indeed, magnetic measurements revealed the impact of this disorder on the macroscopic magnetic behavior. DC susceptibility measurements demonstrated spin-glass-like freezing below 29 K, while a frequency dependent peak at ≈ 80 K in the AC susceptibility suggests slow spin dynamics consistent with cluster glass formation already at high

temperatures.

EXPERIMENTAL METHODOLOGY

Cu_2IrO_3 has been synthesized from its parent material Na_2IrO_3 by using a topotactic reaction [12]. The ion exchange reaction $\text{Na}_2\text{IrO}_3 + 2\text{CuCl} \rightarrow \text{Cu}_2\text{IrO}_3 + 2\text{NaCl}$ replaces the Na^+ with Cu^+ ion. Na_2IrO_3 and CuCl were mixed in a molar ratio of 1:2.2 using a mortar and pestle and then sealed in a quartz tube in an argon atmosphere. The sealed sample was annealed in a muffle furnace for 48 hours at 320°C temperature and then slowly cooled to room temperature at a rate of 1°C per minute. The Cu_2IrO_3 compound is separated from NaCl by washing it in ammonium hydroxide (NH_4OH , Alfa Aesar, 28%) and DI water. The phase purity and stoichiometry of Cu_2IrO_3 was characterized by synchrotron x-ray diffraction (XRD) with $\lambda = 0.20737\text{\AA}$ at Powder Diffraction and Total Scattering Beamline P02.1 at the PETRA III synchrotron at DESY, Hamburg, Germany. The relative stoichiometric ratio Cu:Ir has also been confirmed using energy dispersive x-ray spectroscopy (EDX) mapping with a scanning electron microscope. Local coordination environment was probed using EXAFS at Ir L_3 edge and Cu K edge. The EXAFS spectra were recorded in fluorescence mode at Advanced X-ray Absorption Spectroscopy Beamline P64 at the PETRA III synchrotron at DESY, Hamburg, Germany[22]. Reference absorption edge spectra of materials IrO_2 and CuO were used for energy calibration of incident X-ray in XANES and EXAFS measurement. In order to get better statistics, the EXAFS scans were collected four times and averaged. Normalized XANES spectra and EXAFS oscillations in K -space, $\chi(K)$, were extracted following standard procedures using the ATHENA program[23]. The EXAFS signal, within a selected K -range, was Fourier-transformed to obtain the corresponding R -space spectra, $\chi(R)$. The extracted EXAFS spectra were then analyzed using the ARTEMIS software, which employs ATOMS and FEFF6 to generate theoretical spectra by summing contributions from all possible scattering paths in a given crystallographic structure. Each contribution, such as from the i th coordination shell, was modeled using the standard EXAFS equation with refinable structural parameters, including the coordination number (N_i), average bond length (R_i), and the mean-square relative displacement (MSRD) factor (σ_i^2). These structural parameters were iteratively refined to achieve the best fit between experimental and theoretical spectra. All spectroscopic measurements were performed at 300 K.

The chemical valence state of the elements present in the Cu_2IrO_3 were investigated by X-ray photoelectron spectroscopy (XPS) experiments using Al $K\alpha$ ($h\nu = 1486.7$ eV) laboratory source and hemispherical energy analyzer (Omicron, EA-125, Germany) at the angle in-

egrated photoemission spectroscopy (AIPES) beamline (Indus-1, BL 2, RRCAT, Indore, India). During XPS measurements, experimental chamber vacuum was of the order of 10^{-10} Torr. The charging effect corrections in XPS were done by measuring the C 1s core level spectra. XPS spectra were deconvoluted by fitting with the combined Lorentzian-Gaussian function and Shirley background using XPSPEAK 4.1 program. Soft X-ray absorption spectroscopy has been performed at the MAX-P04 end-station, P04 beamline, Petra III, DESY, Hamburg, Germany. The data was measured with total electron yield (TEY) mode by recording the sample drain current. Room temperature X-ray total scattering measurements were collected at P02.1 (DESY, Hamburg, Germany) with a wavelength of 0.20737\AA and a maximum momentum transfer $Q_{\text{max}} = 25\text{\AA}^{-1}$. The pair distribution function (PDF) was obtained by Fourier transforming the total scattering intensity using the PDFgetX3 program[24]. Structural refinements were performed using PDFgui[25]. DC and AC susceptibility measurements were performed using the Quantum design 9T Evercool (II) Physical Property measurement system (PPMS).

RESULTS AND DISCUSSIONS

X-ray diffraction and elemental analysis

A Rietveld refinement of powder XRD (PXRD) shown in Figure 1 confirmed that the synthesized Cu_2IrO_3 is single phase. The space groups C2/c, P21/c, C2 and C2/m have been used in previous literature as structural models for Cu_2IrO_3 [18, 26]. We attempted a Rietveld refinement of our PXRD data using the above space groups and found that the C2/c space group (No. 15) gives the best fit. The characteristic asymmetric broadening of peaks between 2.43 to 3.43\AA similar to A_2IrO_3 (A: Li, Na) [5, 8] was observed and indicates the presence of stacking faults. The refinement gave the lattice parameters $a = 5.3964\text{\AA}$, $b = 9.3373\text{\AA}$, $c = 11.5204\text{\AA}$, and $\beta = 99.2522^\circ$. The refined fractional atomic coordinates, occupancies, isotropic thermal factors, and the reliability parameter Bragg R-factor obtained is given in Table I. We note that the best refinement gives $\approx 25\%$ antisite disorder between Ir and Cu sites in honeycomb layer.

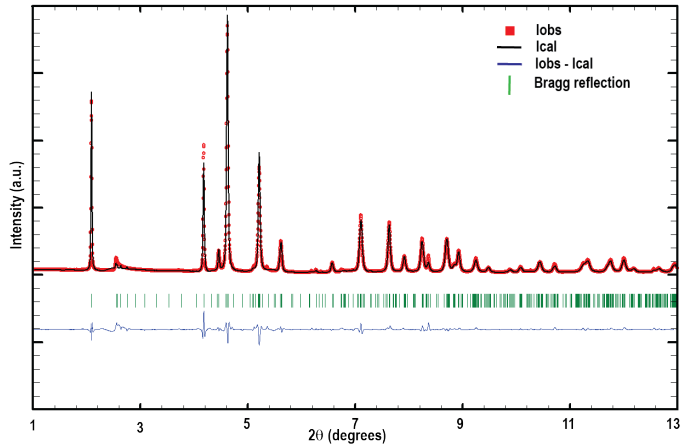


FIG. 1. Rietveld refinement of polycrystalline Cu_2IrO_3 using X-ray data collected at $\lambda = 0.207371\text{\AA}$, confirming that the synthesized powder sample contains no impurity phases.

TABLE I. Refined atomic positions, and occupancies signifying best fit with C2/c space group

Atom	x	y	z	Occupancy	Bragg	R-factor
Ir1	0.2627(4)	0.0809(2)	0	0.75		
Cu1	0.2627(4)	0.0809(2)	0	0.25		3.311
Ir2	0.75	0.25	0	0.5		
Cu2	0.75	0.25	0	0.5		
Cu3	0	0.7334(8)	0.25	1.0		
Cu4	0	0.4455(6)	0.25	1.0		
Cu5	0	0.0803(2)	0.25	1.0		
O1	0.9491(9)	0.75	0.0938(6)	1.0		
O2	0.9492(5)	0.4400(2)	0.0808(6)	1.0		
O3	0.9313(5)	0.0841(2)	0.0880(11)	1.0		

An elemental analysis of the polycrystal Cu_2IrO_3 with energy dispersive x-ray analysis using a scanning electron microscopy gave the Cu: Ir ratio 1.85:1. It is worth noting that no Na was detected in the elemental mapping, suggesting that the parent Na_2IrO_3 phase was fully converted into Cu_2IrO_3 .

CORE LEVEL ELECTRONIC STRUCTURE

X-ray Photoemission and absorption spectroscopy

We have investigated the elemental charge states in Cu_2IrO_3 using X-ray photoemission and soft X-ray absorption measurements. The Cu 2p core-level X-ray photoemission spectra was recorded. Figure 2(a) shows the fitted Cu 2p core splitted as $2p_{1/2}$ and $2p_{3/2}$ due to the spin-orbit splitting. The observed asymmetry and broadening of the spectral features indicate the presence of multiple valence states of Cu. The Cu 2p spectrum was deconvoluted into components centered at 932.2, 934.6, 940.3, 943.2, 952.1, 954.7, and 961.9 eV. The peaks at

932.2 and 952.1 eV correspond to the Cu^{1+} state, while those at 934.6 and 954.7 eV are attributed to Cu^{2+} . The prominent satellite features at 940.3 and 943.2 eV (Cu $2p_{3/2}$ region) and 961.9 eV (Cu $2p_{1/2}$ region) are characteristic signatures of Cu^{2+} [27–30].

The O 1s core-level spectrum was also recorded. Figure 2(b) shows a main peak at 530.2 eV, corresponding to lattice oxygen in Cu_2IrO_3 , along with a higher binding energy feature at 532.2 eV most likely associated with chemisorbed oxygen species such as C–O(H)[27].

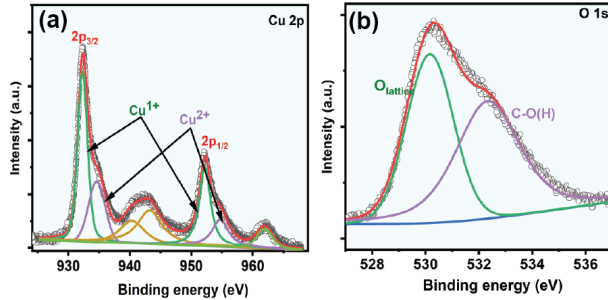


FIG. 2. The deconvoluted Cu 2p and O 1s core-level X-ray photoelectron spectra (XPS) of Cu_2IrO_3 confirming mixed valence state of Cu.

To further confirm this mixed valence nature of Cu observed using photoemission spectra, we measured the XANES spectra across Cu L₃ and L₂ edges, which correspond to the $2p_{3/2} \rightarrow 3d$ and $2p_{1/2} \rightarrow 3d$ electronic transitions, respectively. As shown in Fig. 3, the L₃ edge spectra of Cu_2IrO_3 shows two prominent peaks at 932 eV and 934 eV. The peak at 932 eV closely matches the peak for CuO reference, indicating the presence of Cu^{2+} , while the peak at 934 eV is attributed to Cu^{1+} [11, 27]. Similarly, at the L₂ edge, features are observed at 951.9 eV and 954.9 eV, corresponding to Cu^{2+} and Cu^{1+} , respectively. The coexistence of these features provides clear evidence of a mixed-valent state of copper in Cu_2IrO_3 .

LOCAL STRUCTURE

Extended x-ray absorption spectroscopy

EXAFS measurements at the Ir L₃ and Cu K edges were carried out to probe the local coordination environment, yielding quantitative information on interatomic distances, coordination numbers, and short-range structural disorder. These measurements also enabled determination of the oxidation states of both Ir and Cu. EXAFS is best suited to probe the local effect around scattering center and is sensitive to an order below Å scale [31, 32]. X-ray absorption coefficient as a function of incident photon energy for Ir L₃ edge is shown in Fig. 4. The obtained spectra can be divided into two regions: X-ray

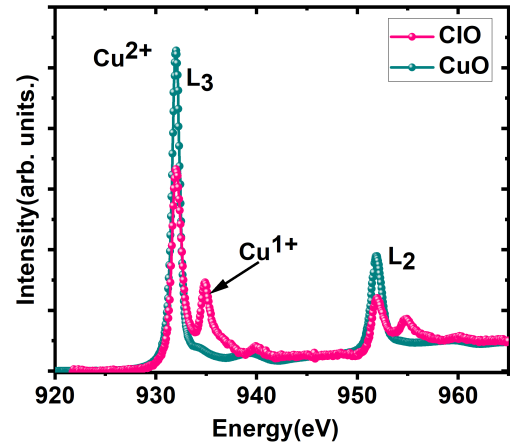


FIG. 3. X-ray absorption spectra at the Cu L-edge for Cu_2IrO_3 and reference CuO. The comparison clearly demonstrates the presence of both Cu^{1+} and Cu^{2+} oxidation states in Cu_2IrO_3 . Distinct spectral features corresponding to the unoccupied 3d states of Cu^{2+} , along with those characteristic of Cu^{1+} , are observed and are marked with arrows in the figure.

Absorption Near-Edge Spectroscopy (XANES) and Extended X-ray Absorption Fine Structure (EXAFS). The XANES region corresponds to the excitation of electrons from the 2p core level to the unoccupied 5d orbital.

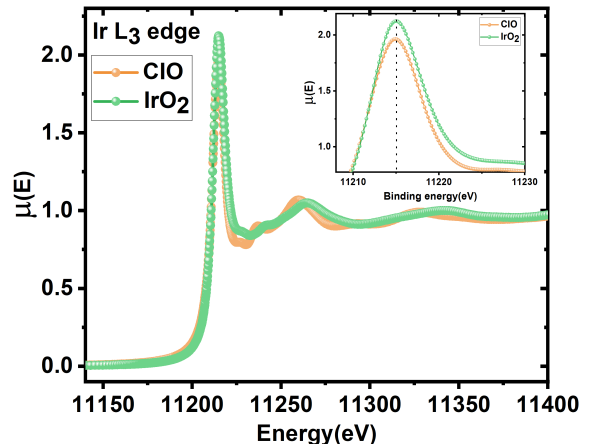


FIG. 4. Normalized XANES spectra at the Ir L₃-edge, with the inset showing a magnified view of the white-line feature. Vertical dashed lines serve as visual guides.

The spectrum of a pure IrO_2 sample in which iridium exists in the 4+ charge state is used as a reference and was simultaneously recorded with Cu_2IrO_3 . The recorded spectrum revealed that the whiteline feature for Cu_2IrO_3 is negative shifted compared to IrO_2 L₃ edge

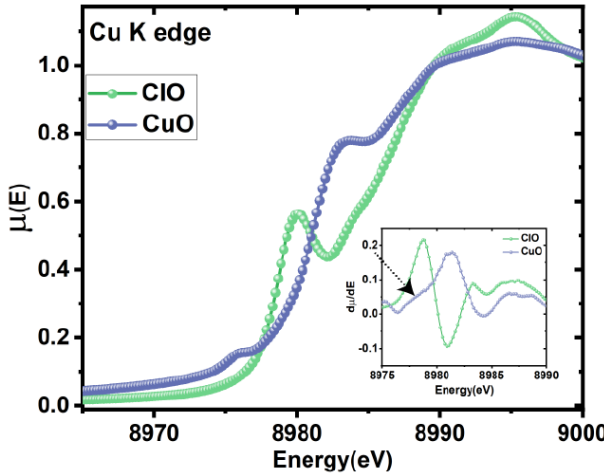


FIG. 5. Normalized XANES spectra at the Cu K-edge, with the inset highlighting the inflection points of the Cu K-edge spectra used to determine the Cu valence state. The analysis indicates that Cu in Cu_2IrO_3 is predominantly in the +1 oxidation state, with a minor contribution from Cu^{2+} , as confirmed by comparison with reference CuO (marked arrow).

as shown in the inset of Fig. 4. Such a shift indicates the presence of a mixed $\text{Ir}^{3+}/\text{Ir}^{4+}$ charge state [33–36]. Cu K edge is also recorded to probe the multivalency of Cu in Cu_2IrO_3 . CuO reference with oxidation state 2+ is measured along with Cu_2IrO_3 . Figure 5 shows the XANES spectra of Cu_2IrO_3 and CuO. Inset shows derivative of absorption coefficient, marked arrow denotes Cu^{2+} charge states in Cu_2IrO_3 along with Cu^{1+} charge states [37, 38]. To explicitly investigate the impact of site disorder, a quantitative analysis of $|\chi(R)|$ was performed by modeling the EXAFS data based on the Cu_2IrO_3 crystal structure ($C2/c$). The fits were constrained to an R range of $1\text{\AA} < R < 3.5\text{\AA}$ and a k range of $3.0\text{\AA}^{-1} < k < 14.5\text{\AA}^{-1}$. Within this region, the EXAFS spectra primarily arise from photoelectron scattering by the nearest-neighbor octahedral O atoms and the second-nearest-neighbor Cu/Ir atoms, which are linked to the Ir core absorber through intermediate O atoms. Based on statistical significance, the most relevant single and multiple scattering paths were incorporated into the theoretical EXAFS model. Along with the Ir-O and Ir-Ir/Cu single-scattering contributions, the Ir-O-O multiple-scattering pathway also contributes significantly.

To define the atomic site disorder (ASD) parameter in the fitting model, two types of structural configurations are considered, both centered around Ir atoms. In the first case, all Ir atoms occupy positions within a hexagonal plane, with Cu atoms located at the center of the hexagonal plaquette, representing a perfectly ordered state. In the second case, Cu and Ir atoms in the honeycomb plane fully exchange sites, and this structure

is treated as the structural limit corresponding to 100% antisite disorder. The theoretical EXAFS spectrum is simulated as a convolution of contributions from these two structural configurations [32, 39].

To determine the fractional contribution from each configuration, the coordination numbers of Ir-Ir_o, Ir-Cu_o, Ir-Ir_d and Ir-Cu_d bonds in both ordered and disordered phase are refined, Ir_o, Cu_o, Ir_d, and Cu_d denote Ir in ordered configuration, Cu in ordered configuration, Ir in disordered configuration and Cu in disordered configuration, respectively.

The ζ_{ASD} parameter quantifies the probability of disordered bond configurations and is expressed as:

$$\zeta_{\text{ASD}} = 1 - q, \quad (1)$$

where

$$q = \frac{N_{\text{Ir-Ir}_o/\text{Cu}_o}}{N_B}, \quad N_B = N_{\text{Ir-Ir}_o} + N_{\text{Ir-Cu}_o} + N_{\text{Ir-Ir}_d} + N_{\text{Ir-Cu}_d}. \quad (2)$$

is probability of ordered bond configuration. Here, $N_{\text{Ir-Ir}_o}$, $N_{\text{Ir-Cu}_o}$, $N_{\text{Ir-Ir}_d}$ and $N_{\text{Ir-Cu}_d}$ represent the coordination numbers of ordered (Ir-Ir_o/Cu_o) and disordered (Ir-Ir_d/Cu_d) bond configurations, respectively, and $N_B = 6$ corresponds to total coordination around the B-site cation, which can be occupied by Ir or Cu under antisite disorder. For Cu_2IrO_3 samples, the total coordination numbers were fixed to crystallographic values.

The amplitude reduction factor (S_0^2) was kept constant at 0.9 [40], a value obtained from the refinement of the Ir L₃-edge EXAFS spectra of IrO_2 . The energy shift (ΔE_0) was also kept consistent across all coordination shells. During refinement, the average coordination distances and mean-square relative displacement (MSRD) factors were optimized. EXAFS is very well modelled using a single Debye-Waller factor and R parameters for each of these Ir-Ir_o/Cu_o and Ir-Ir_d/Cu_d scattering paths.

The quality of fit was assessed using the R factor, defined as:

$$R = \frac{\sum_i [\text{Re}(\chi_d(R_i) - \chi_m(R_i))^2 + \text{Im}(\chi_d(R_i) - \chi_m(R_i))^2]}{\sum_i [\text{Re}(\chi_d(R_i))^2 + \text{Im}(\chi_d(R_i))^2]}, \quad (3)$$

where $\chi_d(R)$ and $\chi_m(R)$ are the experimental and theoretical EXAFS signals, respectively [32, 41]. The best-fit results are superimposed on $k^2\chi(k)$ and $|\chi(R)|$ in Fig. 6(a) and 6 (b). The obtained model patterns show good agreement with the experimental data, as confirmed by the goodness of fit indicator yielding a value of approximately 0.01. The model fitting for the local structure gave bond lengths as Ir-O = 1.938 Å, Ir-Ir_o = 3.177 Å, Ir-Cu_o = 3.130 Å, Ir-Ir_d = 3.067 Å, Ir-Cu_d = 3.067 Å while the estimated ASD fractions for

the sample is 25%. We have also recorded the EXAFS of a sample with slightly less ASD 18% prepared under similar synthesis condition as reported by Abramchuk et.al. [12]. Figure 7 compares the $|\chi(R)|$ of the samples with 25% and 18% ASD. The first peaks show no significant difference between the two patterns, as they primarily correspond to the first nearest-neighbor Ir-O bonds. However, a noticeable change appears in the second peak around 3.2 Å, which has contributions from Ir-Ir and Ir-Cu bonds. The intensity variation between the samples with different amounts of disorder confirms a different neighborhood for the central absorber Ir and hence points to the different fractions of Cu/Ir site mixing in the two samples [42].

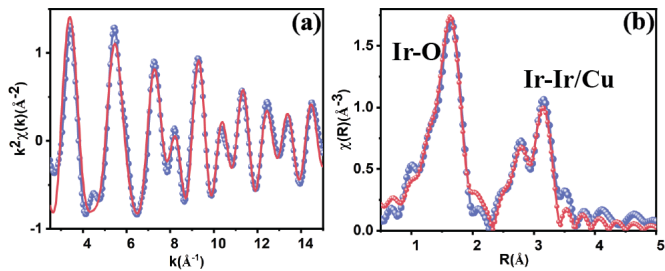


FIG. 6. Ir L₃-edge extended X-ray absorption fine structure (EXAFS) analysis, where the observed data are shown as blue circles and the best-fit results as solid pink lines in both panels: (a) k^2 -weighted spectra $[k^2\chi(k)]$ and (b) corresponding Fourier transform modulus $[\|\chi(R)\|]$ for the Cu₂IrO₃ bulk sample. Contributions from different coordination shells are identified and distinguished across multiple regions of the spectra.

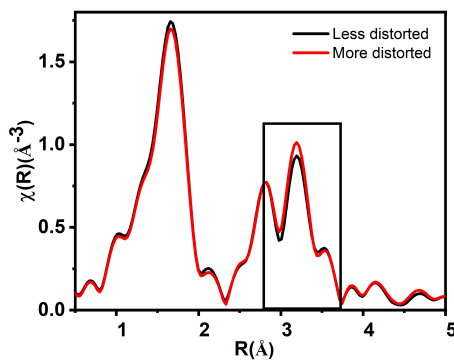


FIG. 7. Fourier transform modulus $[\|\chi(R)\|]$ for a more disordered sample (studied here) and a less disordered sample (studied earlier). The variation in second-shell intensity confirms differences in the fractions of Cu/Ir site mixing.

Pair Distribution Function

To further investigate the local structure and validate the degree of ASD obtained from EXAFS analysis, we performed X-ray pair distribution function (PDF) measurements. This technique is uniquely capable of probing both local and average structural environments. Unlike conventional X-ray diffraction, which yields only the long-range averaged structure from Bragg reflections, PDF analysis incorporates both Bragg and diffuse scattering contributions, enabling the detection of subtle local distortions and antisite cation disorder over the short to intermediate length scales [43–46]. In this work, the PDF data were analyzed over a range extending from 1.5 Å to 30 Å. To quantify the ASD the refinement is first performed with the ideal ordered structural model and then the same data is refined with disordered model (structure obtained from PXRD). Initial long-range refinements (up to 30 Å) were performed to extract the average structure parameters. These parameters were then fixed during the site-occupancy refinements. The Cu and Ir atoms sharing the same crystallographic site were constrained such that their occupancies summed to unity. For the PDF refinements of the disordered structural model, the Cu and Ir occupancies on the mixed 8f site were allowed to be refined simultaneously but with site-multiplicity constraints: if the Cu occupancy on the 8f site is defined as $\text{occ}(\text{Cu})$, the corresponding Ir occupancy on the same site was fixed to $1-\text{occ}(\text{Cu})$. This constraint was applied to all symmetry-equivalent positions of the mixed site. Under this restriction, a fully ordered structure corresponds to zero Cu/Ir ASD. Figure 8(a) shows the refinement using the ordered structural model, which yields a weighted residual factor $R_w = 0.30$. Upon introducing Cu/Ir ASD, R_w is significantly reduced to 0.15, indicating a substantial improvement in the quality of the fit depicted in Fig. 8(c). Similarly, Fig. 8(b) presents the PDF refinement of the local structure assuming zero ASD, yielding a weighted residual factor $R_w = 0.25$. After introducing Cu/Ir ASD, the local-structure PDF refinement shown in Figure 8(d) results in a further reduction of R_w to 0.14, indicating a noticeable improvement in the quality of the fit. Since Ir (Z = 77) and Cu (Z = 29) differ significantly in atomic number, their X-ray atomic form factors ($f(Q)$) differ strongly, providing sufficient scattering contrast to allow the Cu/Ir site occupancies to be distinguished in the PDF. A pronounced reduction in the weighted residual factor (R_w) upon allowing Cu/Ir site mixing to approximately 24.1% (Figure 8), relative to the fully ordered model, supports the amount of disorder estimated previously from PXRD and EXAFS modeling. The peak positions in the real-space $G(r)$ represents the probability of finding an atomic pair separated by a distance r [43]. The shape of a PDF peak provides insight into the distribution of interatomic distances for a given

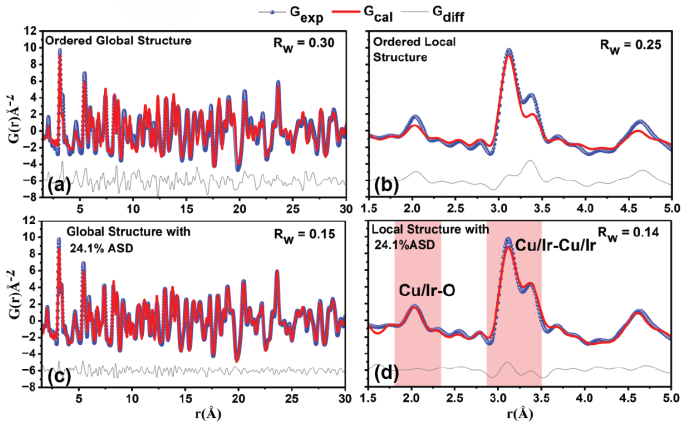


FIG. 8. Room-temperature X-ray PDF of Cu_2IrO_3 tried to fit with ordered structure and ASD. Panels (a,b) show fits using the ordered C2/c model over global (1.5–30 Å) and local (1.5–5 Å) ranges, while (c,d) include 24.1% ASD. G_{exp} denotes the experimental PDF, G_{cal} denotes the calculated PDF from the structural model, and G_{diff} is the difference curve ($G_{\text{exp}} - G_{\text{cal}}$). R_w represents the weighted residual value that quantifies the quality of the fit. Incorporating ASD markedly improves the fit (lower R_w) and better reproduces the local Cu/Ir–O and Cu/Ir–Cu/Ir structures.

atomic pair, whereas its integrated intensity is related to the coordination number[43]. The pink shaded region in Figure 8(d) demonstrates the distribution of coordination pairs in Cu_2IrO_3 .

MAGNETIC PROPERTIES

DC Magnetisation

Figure 9 shows the inverse susceptibility $1/\chi$ measured at $H = 1$ T. At high temperatures ($T > 125$ K) the data can be fit by the Curie-Weiss (CW) law given by

$$\chi = \chi_0 + \frac{C}{T - \theta_{\text{CW}}} \quad (4)$$

where the temperature independent term χ_0 accounts for Van Vleck paramagnetism and diamagnetism of core shells, while C and θ_{CW} represent the Curie constant and Curie-Weiss temperature, respectively. The fit shown as the curve through the data in Figure. 9 yields $C = 28.8$ emu/g, $\chi_0 = -0.016$ emu/g K and $\theta_{\text{CW}} = -203$ K. The negative θ_{CW} indicates the dominance of antiferromagnetic (AFM) interactions in the system. The Curie constant gives an effective magnetic moment $\mu_{\text{eff}} \sim 2.38 \mu_B$, assuming a g -factor $g = 2$. This moment is much larger than the value $1.73 \mu_B$ expected for Ir^{4+} ion with $J = \frac{1}{2}$. This indicates a contribution from Cu^{2+} with $S = 1/2$ although we should be careful in trying to quantify the amount of Cu^{2+} from this enhanced moment

value because in 5d materials strong spin orbit coupling may lead to a larger g -factor which could also lead to an enhanced effective moment compared to the spin-only value. [4, 40, 47].

The low field DC χ from 2 to 300 K measured in zero-field-cooled (ZFC) and field-cooled (FC) modes at different applied magnetic fields H is shown in Figure. 10(a). In low fields $H = 30$ Oe we observe a cusp in ZFC at $T_f = 29$ K and a separation of the ZFC and FC data below this temperature [48, 49]. The $\chi(T)$ measured at different magnetic fields is shown in Figure. 10(a). The T_f shifts towards lower values with magnetic field as shown in the inset of Figure. 10(a) and the bifurcation between ZFC and FC also diminishes with field. These observations are consistent with a frozen spin glass (SG) state below T_f [50].

Magnetic isotherm $M(H)$ measurements were performed at various temperatures, as shown in Figure 10(b). At high temperatures, $M(H)$ exhibits a nearly linear behavior, consistent with the expected response in the paramagnetic (PM) region. However, as the temperature decreases, the magnetization curve develops a noticeable curvature, which becomes more pronounced at lower temperatures, especially below 20 K. At the lowest measured temperature of 2 K, a clear hysteresis is observed, with a coercive field of approximately 1150 Oe shown in inset Figure 10(b). Notably, even at an applied field of 9 T, the magnetization does not reach saturation unlike a ferromagnet, where spins align easily in one direction with applied field. The observation of hysteresis with no saturation till 9 T again suggests SG state, the spins get trapped in metastable energy states [49, 50]. The seemingly hard magnetic properties of spin glasses is usually explained by random anisotropy [50].

To make sense of the observed frozen magnetic state we look to the structural disorder. The magnetic site disorder and the ability of the octahedral coordination in the honeycomb layer to accommodate both Cu^{1+} and Cu^{2+} can lead to the formation of magnetic triangular motifs as shown in Fig. 11. These motifs can introduce frustrated magnetic interactions. Additionally, the competition between different exchange pathways, such as $\text{Ir}^{4+}\text{-O}\text{-Ir}^{4+}$ and $\text{Ir}^{4+}\text{-O}\text{-Cu}^{2+}$, likely plays a significant role in the emergence of glassy magnetic behavior at low temperatures. The ordered magnetic moment per formula unit calculated from $M(H)$ is quite small, only $0.54 \mu_B$ at 9 T in 2 K isotherm $M(H)$.

We would like to get a better understanding of the frozen magnetic state that we observe. Either of spin-glass (SG), cluster spin-glass (CSG), or superparamagnetic (SPM) states can likely lead to the observed glassy behavior at low temperatures. One of the ways to distinguish between these various states is through the temperature dependence of coercivity (H_c) [51]. The variations of H_c and remanent magnetization (M_r) with temperature, determined from the $M(H)$ hysteresis loops, are

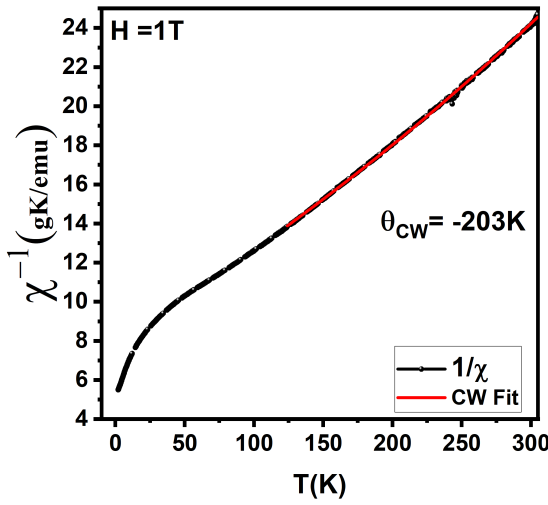


FIG. 9. The temperature dependence of dc magnetic susceptibility of Cu_2IrO_3 , plotted as $\chi^{-1}(T)$ in the temperature range 2-300 K, measured in a field of 1 T. The solid line represents the fit to Curie-Weiss law in the range 125 K to 300 K.

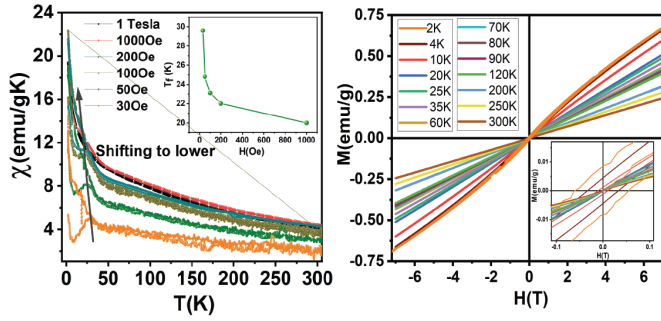


FIG. 10. DC susceptibility measurement (a) ZFC and FC susceptibilities as a function of temperature measured at different applied magnetic field, inset shows variation of T_f with applied magnetic field (b) isothermal magnetisation at various temperatures, inset shows hysteresis loop at lower temperatures below 20 K.

shown in Fig. 12.

For non-interacting SPM systems, H_c is expected to follow the temperature dependence:

$$H_c = H_{c0} \left(1 - \frac{T}{T_B}\right)^{1/2} \quad (5)$$

where H_{c0} represents the coercivity at $T \rightarrow 0$, and T_B is the blocking temperature, defined as the temperature corresponding to the peak in the ZFC $\chi(T)$ curve. As shown in the inset of Fig. 12, the H_c vs $T^{1/2}$ plot exhibits a non-linear behavior, ruling out the SPM blocking as the mechanism for the observed ZFC $\chi(T)$ peak. Instead, the coercivity decreases exponentially with temperature as

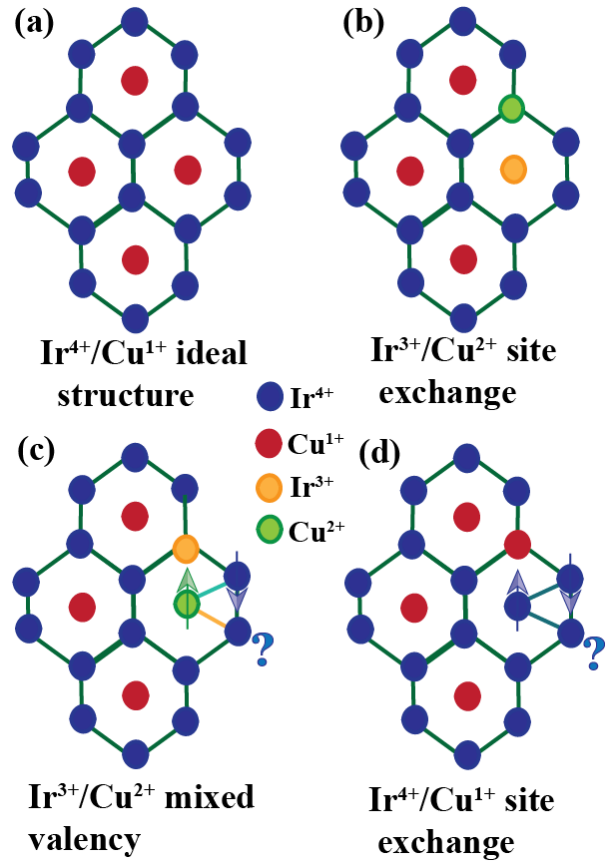


FIG. 11. Schematic representation of possible types of chemical disorders in the honeycomb plane. Cation disorder between Cu^{1+} (red) and Ir^{4+} (blue), along with mixed valency involving Cu^{1+} (Ir^{4+}) and Cu^{2+} (Ir^{3+}) (green (orange)), not only introduces nonmagnetic impurities but also generates new triangular motifs.

shown in the Fig. 12, following an empirical relationship commonly reported for spin-glass and cluster spin-glass systems below the freezing temperature T_f :

$$H_c(T) = H_c(0)e^{-\alpha T} \quad (6)$$

$$M_r(T) = M_r(0)e^{-\beta T} \quad (7)$$

where $H_c(0)$ and $M_r(0)$ represent the coercivity and remanent magnetization at $T = 0$ K, while α and β are phenomenological parameters. The solid curves through the data in Fig. 12 represent fits to the above Eqns. 6 and 7, yielding $H_c(0) = 0.07$ KOe and $\alpha \approx 0.2 \text{ K}^{-1}$ and $M_r(0) = 0.01$ KOe and $\beta \approx 0.2 \text{ K}^{-1}$.

The observed exponential decay of H_c and M_r is consistent with either a spin-glass or a cluster spin-glass state [51].

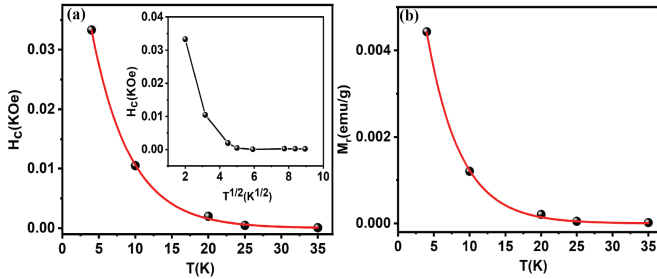


FIG. 12. To differentiate between spin glass (SG), cluster glass, or superparamagnetic (SPM) behavior, the coercivity and retentivity vs. temperature plot follows: (a) Empirical equation (7), with the inset demonstrating a non-linear behavior described by equation (6), ruling out SPM behavior.(b) Empirical equation (7), indicating that Cu_2IrO_3 exhibits characteristics of either SG or cluster glass.

NON EQUILIBRIUM DYNAMICS

We now turn our attention to the non-equilibrium dynamic properties observed in the glassy state below 29 K. We examine the key signatures such as the long-time relaxation of thermoremanent magnetization, as well as memory and rejuvenation effects which are defining traits of spin glass behaviour [51–53].

Magnetic relaxation measurements

To investigate the relaxation behavior, time-dependent magnetization measurements were conducted at various temperatures below freezing temperature $T_f = 29$ K. To investigate the aging (ZFC relaxation) the sample was cooled in zero-field from above T_f to 15 K, and after waiting for a time $t_w = 1000$ s a magnetic field of 100 Oe was applied and the moment versus time was recorded. The resulting time evolution of magnetization, $M(t)$, is shown in Fig. 13. A gradual increase in magnetization over time, known as the magnetic aftereffect, is observed. We can clearly see that the magnetization does not saturate even after 1 hour. This is because, in the glassy state, the moments are randomly frozen and it takes a long time for the field to turn those spins along the field direction. The $M(t, H)$ can be described by the standard stretched exponential expression:

$$M(t, H) = M_0(H) + [M_\infty(H) - M_0(H)] \left[1 - \exp \left(-\frac{t}{\tau} \right)^\alpha \right] \quad (8)$$

where τ represents the characteristic relaxation time, α is the stretching parameter (ranging between 0 and 1), and M_0 and M_∞ are the magnetization values at $t \approx 0$ and $t \rightarrow \infty$, respectively [52, 54, 55]. The best fit parameters obtained for the data at 15 K are $\alpha = 0.48$ and $\tau = 2173$ s. The values of τ and α typically fall in

the range for spin glasses reported earlier [50–53, 56, 57]. The glassy behavior in the Cu_2IrO_3 sample is further supported by FC thermal remanent magnetization (TRM), as shown in Fig. 13 inset. For this measurement the sample was cooled from 300 K to 15 K in 100 Oe and after waiting for 1000 s the field was turned off and the moment versus time was recorded. The time evolution of magnetization can be satisfactorily modeled by Eq. (9). The solid red curves through the data in the Figure represent the best fit, and the obtained fit parameters are $\alpha = 0.58$; $\tau = 1090$ s at 15 K. These values are within the typical range reported for spin-glass systems and are similar to values obtained above from the ZFC relaxation analysis[50–53, 56–58].

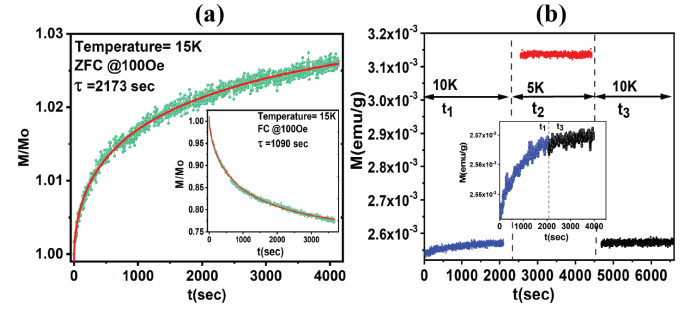


FIG. 13. (a)Relaxation of the ZFC magnetization measured at $T=15$ K, inset shows FC relaxation for same temperature, both fitted using stretched exponential function(red curve)(b) Magnetic relaxation measurements at 10 K with intermediate cooling to 5 K in an applied field of $H = 500$ Oe for ZFC, inset shows magnetization data from intervals 1 and 3 can be merged and seen to be continuous.

Memory effect

The memory effect is another hallmark feature of spin glasses, reflecting their non-equilibrium dynamics and aging phenomena[50–53, 57]. To observe this effect, the sample was ZFC from the paramagnetic state down to 10 K, where a magnetic field of 500 Oe was applied. Similar to relaxation experiments, the magnetization was recorded as a function of time (interval 1). After 40 minutes, the temperature was rapidly decreased to 5 K and maintained for an additional 40 minutes (interval 2), before being increased back to 10 K (interval 3).

The M versus t for the three intervals is shown in Fig. 13(b). The inset shows that the magnetization data from interval-1 and interval-3, both of which are measured at 10 K seamlessly overlap, indicating that the system retains information about its prior state despite the intermediate cooling to 5 K in interval-2. The observed relaxation behavior can be understood within the framework of the hierarchical model of the spin glass state [59, 60]. According to this model, at a given tem-

perature T_0 , the free-energy landscape consists of multiple interconnected valleys. When the sample is cooled from T_0 to $T_0 - \Delta T$, each existing valley further subdivides into smaller sub-valleys, following the hierarchical organization. If ΔT is large, the energy barriers between different valleys become significantly high, restricting relaxation to transitions within the newly formed sub-valleys. Upon reheating the system back to T_0 , these sub-valleys merge, restoring the original energy landscape and thereby demonstrating the memory effect in the decreasing temperature cycle.

AC Magnetisation

AC susceptibility is a tool for investigating the dynamics of spin glasses. A sharp cusp in the real part of the AC susceptibility χ' is usually observed at the freezing temperature (T_f) [50, 61, 62]. The frequency dependence can reveal important information about the glassy state. Below T_f , χ' decreases with increasing frequency, whereas in the paramagnetic regime above T_f , all frequency-dependent curves overlap. A key characteristic of spin glasses is the upward shift of T_f with increasing frequency. In contrast, systems with long-range ferromagnetic or antiferromagnetic order exhibit such frequency-dependent shifts only at much higher frequencies, typically in the MHz range [50].

To investigate the spin glass (SG) dynamics in Cu_2IrO_3 , AC susceptibility measurements were performed in the frequency range of 543 Hz to 9543 Hz, using a fixed excitation field of $H_{\text{ac}} = 10$ Oe, after cooling the sample in zero field. The temperature dependence of χ' is shown in Fig. 14, where a primary peak at T_{f1} is observed along with a smaller shoulder at a lower temperature T_{f2} . We note that in DC χ an anomaly was only observed at T_{f2} . Both peaks observed in ac χ are quite broad unlike the sharp cusps normally observed in canonical spin-glasses. Such broadened peaks suggest the freezing of correlated spin clusters rather than isolated spins. The interactions within these clusters create a distribution of relaxation times, leading to a smoother transition instead of a sharp freezing point [50]. The peak at T_{f1} shifts to higher temperatures with increasing frequency, whereas the shoulder peak at T_{f2} responds only at higher frequencies as shown by the arrows in Fig. 14.

The peak behavior of T_{f1} can be analyzed using the Mydosh parameter, which quantifies the shift in freezing temperature per decade of frequency and is defined as:

$$\delta T_f = \frac{\Delta T_f}{T_f \cdot \Delta \log_{10} \nu}$$

where $\Delta T_f = T_f(\nu_1) - T_f(\nu_2)$ and $\Delta \log_{10} \nu = \log_{10}(\nu_1) - \log_{10}(\nu_2)$.

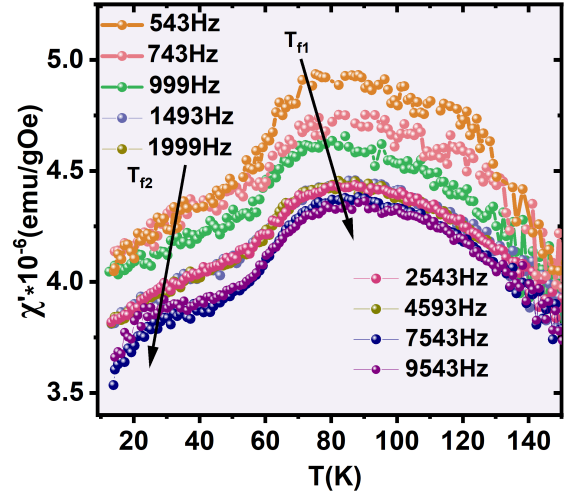


FIG. 14. Temperature dependence of the real part of AC susceptibility (χ') measured at different frequencies. A primary frequency dependent peak is observed at T_{f1} with a smaller shoulder at T_{f2} .

We obtain $\delta T_f \approx 0.089$ which falls between the range characteristic of canonical spin glasses ($\delta T_f \sim 0.005$ for CuMn, $\delta T_f \sim 0.0045$ AuMn) and non-interacting ideal superparamagnets ($\delta T_f \sim 0.28$ for holmium borate glass $\alpha\text{-Ho}_2\text{O}_3(\text{B}_2\text{O}_3)$) [50, 63]. The obtained δT_f is notably larger than that of metallic spin glasses but is comparable to the value found in insulating spin glasses [50]. The much larger value of δT_f compared to canonical spin glasses and the broad anomalies at T_f in ac χ suggest that the system may be best described as a cluster glass, where correlated spin clusters govern the magnetic dynamics.

To distinguish between the spin-glass, cluster glass, and superparamagnetic states, three empirical laws are commonly used to analyze the frequency dependence of T_f :

1. Arrhenius Law:

$$\tau = \tau_0 \exp \left(\frac{E_a}{k_B T_f} \right) \quad (9)$$

This model is typically applicable to non-interacting superparamagnets or weakly interacting magnetic entities.

2. Vogel-Fulcher (VF) Law:

$$\tau = \tau_0 \exp \left[\frac{E_a}{k_B(T_f - T_g)} \right] \quad (10)$$

This approach accounts for interactions between spins.

3. Critical Scaling (CS) Approach:

$$\tau = \tau_0 \left[\frac{T_f}{T_g} - 1 \right]^{-z\nu} \quad (11)$$

Here, τ represents the relaxation time (inverse of the AC frequency) which describes the dynamical fluctuation time scale. T_f is the experimentally determined freezing temperature, τ_0 is the characteristic spin relaxation time (reflecting the timescale of a single spin flip), and E_a represents the activation energy barrier separating metastable states, and T_g is the static freezing temperature as ν approaches zero, while the exponent $z\nu$ characterizes the divergence of the correlation length, defined as

$$\zeta = \left(\frac{T_f}{T_g} - 1 \right)^{-\nu} \quad (12)$$

and k_B is the Boltzmann constant.

The results of parameters obtained from fits to each of these models is summarized in Table II. The inset of Figure 15 (a) demonstrates that the Arrhenius law fails to describe the frequency shift in Cu_2IrO_3 . It does not fit across the entire frequency range, and the extracted parameters ($\tau_0 \approx 8.28 \times 10^{-14}$ s, $E_a/k_B \approx 1615$ K) seems unphysical [53]. We use this to rule out a superparamagnetic state, which also exhibit frequency-dependent T_f behavior but follow the Arrhenius law. The inability of the Arrhenius model to capture the dynamics suggests that the observed behavior is not due to independent spin flips but rather arises from cooperative interactions among spin clusters.

In contrast, both the Vogel-Fulcher and critical-scaling laws, which incorporate the interaction of spins, provide a reasonable fit over the entire frequency range (Figure 15 main panel and inset (b)), supporting the presence of cooperative spins. The Vogel-Fulcher plot yields the parameters E_a/k_B and τ_0 obtained from the slope and intercept of the linear fit. The obtained values are summarised in table II.

Similarly, a plot of $\ln(\tau)$ versus $\ln(T_f/T_g - 1)$, with $T_g = 70$ K (determined from the best fit of data) for critical-scaling approach (inset Figure 15(b)), yields parameters, τ_0 and $z\nu$ from intercept and slope of linear fit. In conventional SG systems, $z\nu$ typically falls within the range 4 to 12, while τ_0 ranges from 10^{-10} to 10^{-13} s for canonical SG and from 10^{-6} to 10^{-10} s for cluster SG [52, 53, 64].

The obtained spin relaxation time for Cu_2IrO_3 , $\tau_0 \approx 10^{-7}$ s and $\tau_0 \approx 10^{-6}$ s from critical scaling and Vogel Fulcher model respectively, falls within the characteristic range for cluster glasses suggesting that in Cu_2IrO_3 spin dynamics occurs in a slow manner, due to the presence of interacting clusters rather than individual spins. The values obtained for τ_0 are similar to those reported in many other cluster- SG systems such as Fe_2O_3 , K_3CrO_3 and Ni doped $\text{La}_{1.85}\text{Sr}_{0.15}\text{CuO}_4$ [65–67]. The extracted critical exponent $z\nu \approx 2.1$ value is also less than the range for usual spin glasses. [55, 66] All these observations taken together suggest that the low temperature frozen state is a cluster-glass instead of a spin-glass. The ratio $k_B T_g/E_a$

obtained from the fit to the Vogel-Fulcher model serves as an indicator of interaction strength between dynamic entities with low values (≤ 1) suggesting weak coupling and higher values (> 1) implying strong coupling [68]. In Cu_2IrO_3 , $k_B T_g/E_a \approx 2.72$, placing the system in the moderate to strong interaction regime. This suggests moderate interactions among the magnetic clusters.

Parameter	Arrhenius	Vogel-Fulcher	Critical Scaling
τ_0 (s)	8.3×10^{-14} $\pm 3.9 \times 10^{-14}$	3.9×10^{-6} $\pm 0.25 \times 10^{-6}$	6.0×10^{-7} $\pm 0.69 \times 10^{-7}$
E_a/k_B (K)	1615 ± 147	25.3 ± 0.5	–
T_{SG} (K)	–	68	70
$z\nu$	–	–	2.10 ± 0.05

TABLE II. Comparison of parameters obtained from Arrhenius, Vogel-Fulcher, and Critical Scaling models.

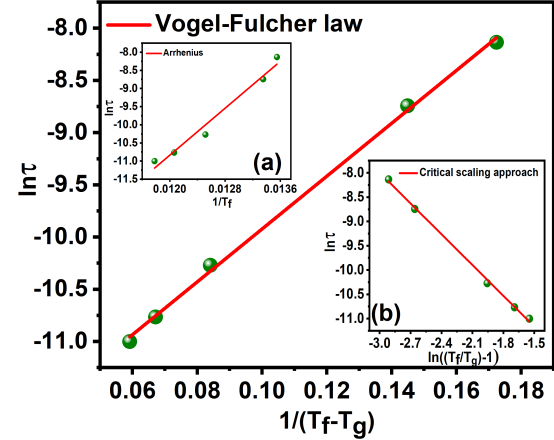


FIG. 15. Fitting the frequency dependence of T_f showing the Vogel-Fulcher law and the critical scaling approach (inset below) both fit equally well, but the Arrhenius law fails (inset above).

Hence our DC and AC susceptibility results conclude that at temperature T_{f1} , dynamically fluctuating AFM clusters are formed [57, 69–71]. The correlated spins within these clusters retain sufficient energy at such high temperatures, preventing static freezing. Dynamic scaling using VF and CS law indicates the correlated behaviour of spins and the strong inter-cluster interactions hinder independent spin freezing, resulting in the cooperative slowing down of relaxation time. As the temperature decreases below T_{f1} , clusters start influencing each other more strongly and become harder to reorient independently eventually driving the system towards cluster freezing. The onset of strictly frozen clusters is observed below 29 K in dc susceptibility, memory and relaxation measurements. Frequency response of T_{f2} shoulder at higher frequency only in ac susceptibility also confirmed

the emergence of static frozen state. Clusters with varying relaxation times respond differently to different frequencies, the response at higher frequencies indicates the presence of clusters with time scales comparable to the applied frequency. Energetically at T_{f2} the cluster behaves as a single large unit, the effective energy barrier is higher enough to flip the correlated spins and clusters freeze together. Since DC susceptibility measures slow, static magnetization changes, it signals the onset of a non-ergodic state at 29K but does not indicate any transition for dynamically fluctuating clusters around 80K. Furthermore, below 20K, a fully frozen state is observed, as evidenced by the emergence of hysteresis, which confirms irreversibility indicating that the clusters remain frozen even when the applied field is cycled.

SUMMARY

We have synthesized Cu_2IrO_3 by an ion exchange reaction of 48 hours at a temperature of 320°C. Using XRD, EXAFS and PDF we quantify approximately 25% atomic disorder within the honeycomb layers of Cu_2IrO_3 . XANES and XPS revealed mixed valence states of Cu and Ir following $\text{Cu}^{1+} + \text{Ir}^{4+} \rightarrow \text{Cu}^{2+} + \text{Ir}^{3+}$. This site disorder and mixed valence introduce complex magnetic interactions in Cu_2IrO_3 , characterized by competing antiferromagnetic (AFM) interactions and frustrated triangular motifs. The AC and DC susceptibility, memory, and relaxation studies indicate the formation of dynamically fluctuating, strongly correlated AFM clusters at approximately 80 K with moderate inter-cluster interactions. Below temperature 29 K, freezing of these clusters sets in. These findings highlight the crucial role of synthesis conditions in governing the structural and magnetic properties of complex oxides. Precisely tuning disorder may be a pathway to engineering emergent quantum phases in strongly correlated oxides.

ACKNOWLEDGEMENT

We thank the X-ray, SEM, and the liquid Helium facilities at IISER Mohali. Y. S. acknowledges support from SERB project CRG/2022/000015 and STARS project STARS-1/240. We acknowledge DESY (Hamburg, Germany), a member of the Helmholtz Association HGF, for the provision of experimental facilities. Parts of this research were carried out at PETRA III, beamline P64, P02.1 and P04 and we thank Dr. Aleksandr Kalinko for beamline guidance at P64 beamline. PY would like to thank Dr. Supriyo Majumdar, Dept. of Material Science and Engineering, Northwestern University, Evanston, Illinois for his useful discussion in analyzing EXAFS section. We would like to thank Dr. R. J. Choudhury UGC-DAE Consortium for Scientific

Research, Indore for X-ray photoemission spectroscopy measurements. Dr. Rajeev Rawat, Kranti Kumar and Somya Shephalika, UGC-DAE Consortium for Scientific Research, Indore, are acknowledged for isothermal MH measurements. We thank Dr. Ashna Bajpai (IISER Pune) for fruitful discussions related to the magnetic study.

- [1] Ji ří Chaloupka, George Jackeli, and Giniyat Khaliullin. Zigzag magnetic order in the iridium oxide Na_2IrO_3 . *Phys. Rev. Lett.*, 110:097204, Feb 2013.
- [2] Alexei Kitaev. Anyons in an exactly solved model and beyond. *Annals of Physics*, 321(1):2–111, 2006. January Special Issue.
- [3] Simon Trebst and Ciarán Hickey. Kitaev materials. *Physics Reports*, 950:1–37, 2022. Kitaev materials.
- [4] G. Jackeli and G. Khaliullin. Mott insulators in the strong spin-orbit coupling limit: From heisenberg to a quantum compass and kitaev models. *Phys. Rev. Lett.*, 102:017205, Jan 2009.
- [5] S. K. Choi, R. Coldea, A. N. Kolmogorov, T. Lancaster, I. I. Mazin, S. J. Blundell, P. G. Radaelli, Yogesh Singh, P. Gegenwart, K. R. Choi, S.-W. Cheong, P. J. Baker, C. Stock, and J. Taylor. Spin waves and revised crystal structure of honeycomb iridate Na_2IrO_3 . *Phys. Rev. Lett.*, 108:127204, Mar 2012.
- [6] Yogesh Singh, S. Manni, J. Reuther, T. Berlijn, R. Thomale, W. Ku, S. Trebst, and P. Gegenwart. Relevance of the heisenberg-kitaev model for the honeycomb lattice iridates $A_2\text{IrO}_3$. *Phys. Rev. Lett.*, 108:127203, Mar 2012.
- [7] R. D. Johnson, S. C. Williams, A. A. Haghaghian, J. Singleton, V. Zapf, P. Manuel, I. I. Mazin, Y. Li, H. O. Jeschke, R. Valentí, and R. Coldea. Monoclinic crystal structure of α -RuCl₃ and the zigzag antiferromagnetic ground state. *Phys. Rev. B*, 92:235119, Dec 2015.
- [8] S. C. Williams, R. D. Johnson, F. Freund, Sungkyun Choi, A. Jesche, I. Kimchi, S. Manni, A. Bombardi, P. Manuel, P. Gegenwart, and R. Coldea. Incommensurate counterrotating magnetic order stabilized by kitaev interactions in the layered honeycomb α -Li₂IrO₃. *Phys. Rev. B*, 93:195158, May 2016.
- [9] Sean K. Takahashi, Jiaming Wang, Alexandre Arsenault, Takashi Imai, Mykola Abramchuk, Fazel Tafti, and Philip M. Singer. Spin excitations of a proximate kitaev quantum spin liquid realized in Cu_2IrO_3 . *Phys. Rev. X*, 9:031047, Sep 2019.
- [10] Y. S. Choi, C. H. Lee, S. Lee, Sungwon Yoon, W.-J. Lee, J. Park, Anzar Ali, Yogesh Singh, Jean-Christophe Orain, Gareoung Kim, Jong-Soo Rhyee, Wei-Tin Chen, Fangcheng Chou, and Kwang-Yong Choi. Exotic low-energy excitations emergent in the random kitaev magnet Cu_2IrO_3 . *122:167202*, Apr 2019.
- [11] Eric M. Kenney, Carlo U. Segre, William Lafargue-Dit-Hauret, Oleg I. Lebedev, Mykola Abramchuk, Adam Berlie, Stephen P. Cottrell, Gediminas Simutis, Faranak Bahrami, Natalia E. Mordinova, Gilberto Fabbris, Jessica L. McChesney, Daniel Haskel, Xavier Rocquefelte, Michael J. Graf, and Fazel Tafti. Coexistence of static

and dynamic magnetism in the kitaev spin liquid material Cu_2IrO_3 . *Phys. Rev. B*, 100:094418, Sep 2019.

[12] Mykola Abramchuk, Cigdem Ozsoy-Keskinbora, Jason W. Krizan, Kenneth R. Metz, David C. Bell, and Fazel Tafti. Cu_2IrO_3 : A new magnetically frustrated honeycomb iridate. *Journal of the American Chemical Society*, 139(43):15371–15376, 2017. PMID: 28981260.

[13] Ying Li, Stephen M. Winter, and Roser Valentí. Role of hydrogen in the spin-orbital-entangled quantum liquid candidate $H_3\text{LiIr}_2\text{O}_6$. *Phys. Rev. Lett.*, 121:247202, Dec 2018.

[14] Yuya Haraguchi, Daisuke Nishio-Hamane, Akira Matsuo, Koichi Kindo, and Hiroko Aruga Katori. High-temperature magnetic anomaly via suppression of antisite disorder through synthesis route modification in a kitaev candidate Cu_2IrO_3 . *Journal of Physics: Condensed Matter*, 36(40):405801, jul 2024.

[15] Zhenyue Zhu, P. A. Maksimov, Steven R. White, and A. L. Chernyshev. Disorder-induced mimicry of a spin liquid in YbMgGaO_4 . *Phys. Rev. Lett.*, 119:157201, Oct 2017.

[16] Hiroaki Ishizuka. Temperature-dependent magnetic anisotropy from pseudo-dipolar interactions. *Phys. Rev. B*, 95:184413, May 2017.

[17] Srishti Pal, Arnab Seth, Piyush Sakrikar, Anzar Ali, Subhro Bhattacharjee, D. V. S. Muthu, Yogesh Singh, and A. K. Sood. Probing signatures of fractionalization in the candidate quantum spin liquid Cu_2IrO_3 via anomalous raman scattering. *Phys. Rev. B*, 104:184420, Nov 2021.

[18] Ying Li, Roger Johnson, Yogesh Singh, Radu Coldea, and Roser Valentí. Origin of the insulating state in the kitaev candidate Cu_2IrO_3 . *arXiv*, 2024.

[19] Hironori Kobayashi, Mitsuharu Tabuchi, Masahiro Shikano, Hiroyuki Kageyama, and Ryoji Kanno. Structure, and magnetic and electrochemical properties of layered oxides, Li_2IrO_3 . *Journal of Materials Chemistry - J MATER CHEM*, 13:957–962, 03 2003.

[20] Florian Freund, S. Williams, Radu Coldea, Philipp Gegenwart, and Anton Jesche. Single crystal growth from separated educts and its application to lithium transition-metal oxides. *Scientific Reports*, 6, 04 2016.

[21] Faranak Bahrami, Eric M. Kenney, Chennan Wang, Adam Berlie, Oleg I. Lebedev, Michael J. Graf, and Fazel Tafti. Effect of structural disorder on the kitaev magnet $\text{Ag}_3\text{LiIr}_2\text{O}_6$. *Phys. Rev. B*, 103:094427, Mar 2021.

[22] Wolfgang A. Caliebe, Vadim Murzin, Aleksandr Kalinko, and Marcel Görlitz. High-flux xafs-beamline p64 at petra iii. *AIP Conference Proceedings*, 2054(1):060031, 01 2019.

[23] B. Ravel and M. Newville. ATHENA, ARTEMIS, HEP-HAESTUS: data analysis for X-ray absorption spectroscopy using IFEFFIT. *Journal of Synchrotron Radiation*, 12(4):537–541, Jul 2005.

[24] P. Juhás, T. Davis, C. L. Farrow, and S. J. L. Billinge. Pdfgetx3: a rapid and highly automatable program for processing powder diffraction data into total scattering pair distribution functions. *Journal of Applied Crystallography*, 46(2):560–566, 2013.

[25] C Farrow, P Juhás, J Liu, D Bryndin, Emil Bozin, Jacques Bloch, Th Proffen, and Simon Billinge. Pdfit2 and pdfgui: Computer programs for studying nanostructure in crystals. *Journal of physics. Condensed matter : an Institute of Physics journal*, 19:335219, 08 2007.

[26] G. Fabbris, A. Thorn, W. Bi, M. Abramchuk, F. Bahrami, J. H. Kim, T. Shimmei, T. Irifune, F. Tafti, A. N. Kolmogorov, and D. Haskel. Complex pressure-temperature structural phase diagram of the honeycomb iridate Cu_2IrO_3 . *Phys. Rev. B*, 104:014102, Jul 2021.

[27] Hemant Singh Kunwar, Isha, Arvind Kumar Yogi, Binoy Krishna De, Vivek Dwij, Mayanak Kumar Gupta, R. Mittal, R. Venkatesh, R. J. Chaudhary, Mahesh Vedpathak, and V. G. Sathe. Raman scattering of spin- $\frac{1}{2}$ mixed-dimensionality antiferromagnetic $\alpha\text{-Cu}_2\text{V}_2\text{O}_7$. *Phys. Rev. B*, 109:054310, Feb 2024.

[28] Dahlang Tahir and Sven Tougaard. Electronic and optical properties of Cu, CuO and Cu_2O studied by electron spectroscopy. *Journal of Physics: Condensed Matter*, 24(17):175002, apr 2012.

[29] Davide Barreca, Alberto Gasparotto, and Eugenio Tondello. CVD Cu_2O and CuO nanosystems characterized by xps. *Surface Science Spectra*, 14(1):41–51, 07 2009.

[30] R. P. Vasquez. CuO by XPS. *Surface Science Spectra*, 5(4):262–266, 10 1998.

[31] Badari Narayana Rao, Luca Olivi, Vasant Sathe, and Rajeev Ranjan. Electric field and temperature dependence of the local structural disorder in the lead-free ferroelectric $\text{Na}_{0.5}\text{Bi}_{0.5}\text{TiO}_3$: An exafs study. *Phys. Rev. B*, 93:024106, Jan 2016.

[32] Supriyo Majumder, Malvika Tripathi, R. Raghunathan, P. Rajput, S. N. Jha, D. O. de Souza, L. Olivi, S. Chowdhury, R. J. Choudhary, and D. M. Phase. Mapping the magnetic state as a function of antisite disorder in $\text{Sm}_2\text{NiMnO}_6$ double perovskite thin films. *Phys. Rev. B*, 105:024408, Jan 2022.

[33] E. Paris, B. Joseph, A. Iadecola, C. Marini, K. Kudo, D. Mitsuoka, M. Nohara, T. Mizokawa, and N. L. Saini. Determination of temperature-dependent atomic displacements in the $\text{Ca}_{10}\text{Ir}_4\text{As}_8(\text{Fe}_2\text{As}_2)_5$ superconductor with a metallic spacer layer. *Phys. Rev. B*, 90:094508, Sep 2014.

[34] Jie Cheng, Xuanyong Sun, Shengli Liu, Bin Li, Haiyun Wang, Peng Dong, Yu Wang, and Wei Xu. La-doping effect on spin-orbit coupled Sr_2IrO_4 probed by x-ray absorption spectroscopy. *New Journal of Physics*, 18(9):093019, sep 2016.

[35] M. K. Wallace, Jun Li, P. G. Labarre, S. Svalenak, D. Haskel, J. Kim, G. E. Sterbinsky, F. Rodolakis, H. Park, A. P. Ramirez, and M. A. Subramanian. Structural and electronic properties of the first iridium containing mixed b-site spinel oxide: $\text{CuIr}_{1.5}\text{Cu}_{0.5}\text{O}_4$. *Phys. Rev. Mater.*, 5:094410, Sep 2021.

[36] Priyanka Yadav, Sumit Sarkar, Manju Sharma, Deodatta Phase, Ram Janay Choudhary, and Rajamani Raghunathan. Role of local structural distortions on the origin of $j = 1/2$ pseudo- spin state in sodium iridate. *ACS Applied Electronic Materials*, 01 2023.

[37] H. C. Wu, Y. C. Chung, T. W. Yen, H. J. Chen, T. W. Kuo, D. Chandrasekhar Kakarla, S. M. Huang, Y.-Y. Wang, J.-Y. Lin, J. J. Lee, Y. C. Lai, C. L. Chen, J. F. Lee, T. L. Chou, Y.-C. Lai, M.-W. Chu, Mitch M. C. Chou, and H. D. Yang. Evidence of a structural phase transition in the triangular-lattice compound CuIr_2Te_4 . *Phys. Rev. B*, 103:104111, Mar 2021.

[38] Wen-Zhu Yu, Wei-Wei Wang, Shan-Qing Li, Xin-Pu Fu, Xu Wang, Ke Wu, Rui Si, Chao Ma, Chun-Jiang Jia, and Chun-Hua Yan. Construction of active site in a sintered copper-ceria nanorod catalyst. *Journal of the*

American Chemical Society, 141(44):17548–17557, 2019. PMID: 31607122.

[39] C. Meneghini, Sugata Ray, F. Liscio, F. Bardelli, S. Mombilio, and D. D. Sarma. Nature of “disorder” in the ordered double perovskite Sr_2FeMoO_6 . *Phys. Rev. Lett.*, 103:046403, Jul 2009.

[40] Priyanka Yadav, Sumit Sarkar, Manju Sharma, Deodatta Moreshwar Phase, Ram Janay Choudhary, and Rajamani Raghunathan. Role of local structural distortions on the origin of $j = 1/2$ pseudo-spin state in sodium iridate. *ACS Applied Electronic Materials*, 5(1):418–428, 2023.

[41] S. D. Kelly, D. Hesterberg, and B. Ravel. *Analysis of Soils and Minerals Using X-ray Absorption Spectroscopy*, chapter 14, pages 387–463. John Wiley & Sons, Ltd, 2008.

[42] Badari Narayana Rao, Luca Olivi, Vasant Sathe, and Rajeet Ranjan. Electric field and temperature dependence of the local structural disorder in the lead-free ferroelectric $Na_{0.5}Bi_{0.5}TiO_3$: An EXAFS study. *Phys. Rev. B*, 93:024106, Jan 2016.

[43] Takeshi Egami and Simon Billinge. Underneath the bragg peaks. *Materials Today - MATER TODAY*, 6:57–57, 06 2003.

[44] Valeri Petkov. *Pair Distribution Functions Analysis*, pages 1–14. John Wiley & Sons, Ltd, 2012.

[45] Th Proffen, Simon Billinge, Takeshi Egami, and Despina Louca. Structural analysis of complex materials using the atomic pair distribution function – a practical guide. *Zeitschrift Fur Kristallographie - Z KRISTALLOGR*, 218, 02 2003.

[46] P. Juhás, T. Davis, C. L. Farrow, and S. J. L. Billinge. *PDFgetX3*: a rapid and highly automatable program for processing powder diffraction data into total scattering pair distribution functions. *Journal of Applied Crystallography*, 46(2):560–566, Apr 2013.

[47] C. H. Sohn, H.-S. Kim, T. F. Qi, D. W. Jeong, H. J. Park, H. K. Yoo, H. H. Kim, J.-Y. Kim, T. D. Kang, Deok-Yong Cho, G. Cao, J. Yu, S. J. Moon, and T. W. Noh. Mixing between $J_{\text{eff}} = \frac{1}{2}$ and $\frac{3}{2}$ orbitals in Na_2iro_3 : A spectroscopic and density functional calculation study. *Phys. Rev. B*, 88:085125, Aug 2013.

[48] Gyanendra Panchal, Reshu Choudhary, Manish Kumar, and D. Phase. Interfacial spin glass mediated spontaneous exchange bias effect in self-assembled $La_{0.7}Sr_{0.3}MnO_3:NiO$ nanocomposite thin films. *Journal of Alloys and Compounds*, 05 2019.

[49] K. Binder and A. P. Young. Spin glasses: Experimental facts, theoretical concepts, and open questions. *Rev. Mod. Phys.*, 58:801–976, Oct 1986.

[50] J. A. Mydosh. In *Spin glasses:an experimental introduction*, 1993.

[51] Arun Kumar and Dhananjai Pandey. Study of magnetic relaxation, memory and rejuvenation effects in the cluster spin-glass phase of b-site disordered $CaFe_{0.5}Nb_{0.5}O_3$ perovskite: Experimental evidence for hierarchical model. *Journal of Magnetism and Magnetic Materials*, 511:166964, 2020.

[52] Johannes Kroder, Kaustuv Manna, Dominik Kriegner, A. S. Sukhanov, Enke Liu, Horst Borrman, Andreas Hoser, Johannes Gooth, Walter Schnelle, Dmytro S. Inosov, Gerhard H. Fecher, and Claudia Felser. Spin glass behavior in the disordered half-heusler compound $irmga$. *Phys. Rev. B*, 99:174410, May 2019.

[53] Pallab Bag, P. R. Baral, and R. Nath. Cluster spin-glass behavior and memory effect in $Cr_{0.5}Fe_{0.5}Ga$. *Phys. Rev. B*, 98:144436, Oct 2018.

[54] Deena Nath, Sujay Chakravarty, K. Saravanan, U.P. Deshpande, Arup Dasgupta, A.V. Thanikai Arasu, R. Baskaran, and N.V. Chandra Shekar. Thermally-induced co-existence of superparamagnetism and spin-glass like behavior in undoped amorphous aln thin film. *Materials Research Bulletin*, 153:111876, 2022.

[55] T Chakrabarty, A V Mahajan, and S Kundu. Cluster spin glass behavior in geometrically frustrated $Zn_3V_3O_8$. *Journal of Physics: Condensed Matter*, 26(40):405601, sep 2014.

[56] Santanu Pakhira, Chandan Mazumdar, R. Ranganathan, S. Giri, and Maxim Avdeev. Large magnetic cooling power involving frustrated antiferromagnetic spin-glass state in $R_2NiSi_3(R = Gd, Er)$. *Phys. Rev. B*, 94:104414, Sep 2016.

[57] C. A. Cardoso, F. M. Araujo-Moreira, V. P. S. Awana, E. Takayama-Muromachi, O. F. de Lima, H. Yamuchi, and M. Karppinen. Spin glass behavior in $RuSr_2Gd_{1.5}Ce_{0.5}Cu_2O_{10-\delta}$. *Phys. Rev. B*, 67:020407, Jan 2003.

[58] R. Kolay, A. Magar, A. A. Tsirlin, and R. Nath. Cluster-glass behavior and large magnetocaloric effect in the frustrated hyperkagome ferromagnet $Li_2MgMn_3O_8$. *Phys. Rev. B*, 111:104403, Mar 2025.

[59] V S Dotsenko. Fractal dynamics of spin glasses. *Journal of Physics C: Solid State Physics*, 18(32):6023, nov 1985.

[60] F. Lefloch, J. Hammann, M. Ocio, and E. Vincent. Can aging phenomena discriminate between the droplet model and a hierarchical description in spin glasses? *Europhysics Letters*, 18(7):647, apr 1992.

[61] V. Cannella and J. A. Mydosh. Magnetic ordering in gold-iron alloys. *Phys. Rev. B*, 6:4220–4237, Dec 1972.

[62] J. I. Budnick, V. Cannella, and T. J. Burch. Low field magnetic susceptibility of $(Pd_{1-x}Ag_x)_{0.99}Fe_{0.01}$. *AIP Conference Proceedings*, 18(1):307–311, 03 1974.

[63] C. A. M. Mulder, A. J. van Duyneveldt, and J. A. Mydosh. Frequency and field dependence of the ac susceptibility of the $AuMn$ spin-glass. *Phys. Rev. B*, 25:515–518, Jan 1982.

[64] Anuj Kumar, R. P. Tandon, and V. P. S. Awana. Study of spin glass and cluster ferromagnetism in $RuSr_2Gd_{1.5}Ce_{0.5}Cu_2O_{10-\delta}$ magneto superconductor. *Journal of Applied Physics*, 110(4):043926, 08 2011.

[65] M. D. Mukadam, S. M. Yusuf, P. Sharma, S. K. Kulshreshtha, and G. K. Dey. Dynamics of spin clusters in amorphous Fe_2O_3 . *Phys. Rev. B*, 72:174408, Nov 2005.

[66] Lilia D. Kulish and Graeme R. Blake. Static and dynamic magnetic properties of K_3CrO_4 . *Journal of Magnetism and Magnetic Materials*, 537:168213, 2021.

[67] A. Malinowski, V. L. Bezusyy, R. Minikayev, P. Dziawa, Y. Syryanyy, and M. Sawicki. Spin-glass behavior in ni-doped $La_{1.85}Sr_{0.15}CuO_4$. *Phys. Rev. B*, 84:024409, Jul 2011.

[68] S. Shtrikman and E.P. Wohlfarth. The theory of the vogel-fulcher law of spin glasses. *Physics Letters A*, 85(8):467–470, 1981.

[69] Kostya Trachenko. Understanding the spin glass transition as a dynamic phenomenon. *Journal of Physics: Condensed Matter*, 23(36):366003, aug 2011.

[70] Ajaya K Nayak, K G Suresh, and A K Nigam. Correlation between reentrant spin glass behavior and the magnetic

order-disorder transition of the martensite phase in Ni-Co-Mn-Sb heusler alloys. *Journal of Physics: Condensed Matter*, 23(41):416004, sep 2011.

[71] R. S. Freitas, L. Ghivelder, F. Damay, F. Dias, and L. F. Cohen. Magnetic relaxation phenomena and cluster glass properties of $La_{0.7-x}Y_xCa_{0.3}MnO_3$ manganites. *Phys. Rev. B*, 64:144404, Sep 2001.